Nanoscale

COMMUNICATION

View Article Online
View Journal | View Issue

Cite this: *Nanoscale*, 2016, **8**, 1897

Received 24th September 2015,
Accepted 27th December 2015

DOI: 10.1039/c5nr06602f

www.rsc.org/nanoscale

Construction of a 3D rGO–collagen hybrid scaffold for enhancement of the neural differentiation of mesenchymal stem cells†

Weibo Guo,[a,b] Shu Wang,[a,b] Xin Yu,[a,b] Jichuan Qiu,[c] Jianhua Li,[c] Wei Tang,[c] Zhou Li,[a] Xiaoning Mou,*[a] Hong Liu*[a,c] and Zhonglin Wang[a,d]

The cell–material interface is one of the most important considerations in designing a high-performance tissue engineering scaffold because the surface of the scaffold can determine the fate of stem cells. A conductive surface is required for a scaffold to direct stem cells toward neural differentiation. However, most conductive polymers are toxic and not amenable to biological degradation, which restricts the design of neural tissue engineering scaffolds. In this study, we used a bioactive three-dimensional (3D) porcine acellular dermal matrix (PADM), which is mainly composed of type I collagen, as a basic material and successfully assembled a layer of reduced graphene oxide (rGO) nanosheets on the surface of the PADM channels to obtain a porous 3D, biodegradable, conductive and biocompatible PADM–rGO hybrid neural tissue engineering scaffold. Compared with the PADM scaffold, assembling the rGO into the scaffold did not induce a significant change in the microstructure but endowed the PADM–rGO hybrid scaffold with good conductivity. A comparison of the neural differentiation of rat bone-marrow-derived mesenchymal stem cells (MSCs) was performed by culturing the MSCs on PADM and PADM–rGO scaffolds in neuronal culture medium, followed by the determination of gene expression and immunofluorescence staining. The results of both the gene expression and protein level assessments suggest that the rGO-assembled PADM scaffold may promote the differentiation of MSCs into neuronal cells with higher protein and gene expression levels after 7 days under neural differentiation conditions. This study demonstrated that the PADM–rGO hybrid scaffold is a promising scaffold for neural tissue engineering; this scaffold can not only support the growth of MSCs at a high proliferation rate but also enhance the differentiation of MSCs into neural cells.

[a]*Beijing Institute of Nanoenergy and Nanosystems, Chinese Academy of Sciences, National Center for Nanoscience and Technology (NCNST), Beijing, 100083, P. R. China. E-mail: mouxiaoning@163.com, hongliu@sdu.edu.cn*
[b]*University of Chinese Academy of Sciences, Beijing, 100049, P. R. China*
[c]*State Key Laboratory of Crystal Materials, Shandong University, Jinan, 250100, P. R. China*
[d]*School of Materials Science and Engineering, Georgia Institute of Technology, Atlanta, Georgia 30332-0245, USA*
†Electronic supplementary information (ESI) available. See DOI: 10.1039/c5nr06602f

1. Introduction

The regeneration of a damaged nervous system is still a major challenge in the field of neuroscience.[1] Tissue engineering, which is based on seeded cells, growth factors and scaffolds, is one of the most promising approaches in regenerative medicine, which aims to restore or enhance tissue and organ functions.[2] In particular, the success of neural tissue engineering mainly relies on the regulation of stem cell behavior and the progression of tissue through the scaffold. Generally, the scaffold for neural tissue engineering should be analogous to the natural extracellular matrix (ECM) with appropriate mechanical properties, biocompatibility, conductivity, controllable degradability with non-toxic degradation products, a porous structure for cell adhesion and migration, and the ability to support a three-dimensional (3D) cell culture.[3,4]

Recently, numerous natural and synthetic materials have been investigated for the fabrication of scaffolds for neural tissue engineering. Nanostructured porous poly(L-lactic acid) (PLA),[5] poly(glycolic acid) (PGA),[6] and their co-polymer, poly(L-lactic acid)-*co*-poly(glycolic acid) (PLA–PGA),[7] have been intensively studied for neural tissue engineering scaffold applications because these polymers are formable and easy to scale up. However, these synthetic polymers could rapidly release and accumulate acidic degradation products, which would result in a more rapid decrease in the pH of the surrounding milieu and decrease the *in vivo* biocompatibility.[8,9] Certain natural polymer scaffolds, such as collagen, gelatin and silk fibroin,[10] have attracted much attention because of their biocompatibility and bioactivity. However, natural and synthetic polymers cannot meet all the requirements of an ideal scaffold because natural polymers often lose their mechanical properties very early during degradation, which makes it difficult to regulate the morphology of the newly generated nerve.[11] During the past decade, many efforts have been devoted to designing decellularized tissues and organs for tissue engineering.[12,13] Although a decellularized neural tissue matrix would be the best choice for a neural tissue engineering scaffold, the limitation of this tissue resource is a great

obstacle for the practical application of this type of scaffold. As a type of natural ECM, porcine acellular dermal matrix (PADM) is a promising natural polymer scaffold for nerve regeneration. PADM is derived from porcine skin by removing cells and cellular components, leaving only the native structure of the dermal meshwork, and is mainly composed of type I collagen, with a small amount of type II collagen.[14] As provided, PADM possesses excellent biocompatibility, bioactivity, controllable biodegradability *via* cross-linking, a porous structure that is similar to the ECM, and an immunogenicity similar to the human acellular dermal matrix. PADM has been successfully applied in skin tissue engineering, covering full thickness burn wounds in clinical practice, and bone tissue engineering studies.[15,16] PADM thus appears to be a good choice for a neural tissue engineering scaffold. However, PADM does not fulfill another important requirement to qualify as a neural tissue engineering scaffold, *i.e.* good conductivity of the material.[17] Therefore, improving the conductivity of the materials has become the major challenge in designing a scaffold for neural tissue engineering.[18] Graphene, a zero-band two-dimensional (2D) monolayered carbon material, has attracted the attention of scientists and engineers in many fields due to the perfect physical, chemical, thermal, and mechanical properties of this material.[19] Most recently, graphene oxide (GO), which is chemically exfoliated from bulk graphite, has attracted much attention from biomaterials scientists and biomedical engineers because of its biocompatibility and biodegradation ability.[20] Graphene-related materials have been used in many biomedical applications, including cellular imaging, drug delivery, and stem cell research, and have the potential for neural interfacing.[21] However, bulk graphene-based porous structures, normally synthesized from GO, possess drawbacks, such as low strength and too small pores, resulting in low cell adhesion and slow migration on these surfaces.[22] Prof. Loh and co-workers demonstrated that graphene films can be used to enhance cell adhesion and neural differentiation of mesenchymal stem cells (MSCs).[23] Therefore, based on the above discussion, assembling a graphene layer on the surface of porous PADM channels to combine the advantages of both the high strength and high bioactivity of PADM with the high electric conductivity of graphene should be one of the best approaches for manufacturing high-performance neural tissue engineering scaffolds.

As mentioned above, stem cells play a pivotal role in tissue engineering and modern regenerative medicine.[24] As one of the most important seed cells for tissue engineering, bone-marrow-derived MSCs have the potential to differentiate into various cell types, including adipocytes, osteoblasts and chondrocytes,[24] cardiac muscle cells,[25] hepatocytes[26] and neural cells.[27] Compared with neural stem cells, because of the ease of isolation of MSCs and the abundant sources of these cells, bone-marrow-derived MSCs have generated great interest regarding their potential application to neural regenerative medicine.[28] By combining neural differentiation protocols with growth factors,[29] the effects of the conductive properties of materials on the neural differentiation of MSCs can be studied.[30]

In this study, we successfully assembled a layer of reduced graphene oxide (rGO) nanosheets on the surface of porous PADM channels to form a conductive, porous, 3D PADM–rGO hybrid neural tissue engineering scaffold. MSCs were used as seed cells to determine whether the variation in conductivity caused by the rGOs can affect the neural differentiation of MSCs. The results demonstrated that the rGO-assembled PADM not only maintains the porous 3D structure and good cytocompatibility but also enables a delay in the biodegradation rate and greatly improves the conductivity of the PADM. Most importantly, the porous, 3D PADM–rGO hybrid neural tissue engineering scaffold with high conductivity can enhance neuronal differentiation under neural differentiation conditions for 7 days, as demonstrated by the assessment of protein and gene expression levels. This work opens a facile approach to designing and preparing a conductive biopolymer-based porous 3D scaffold. This type of scaffold has great potential in neural tissue engineering.

2. Results and discussion

2.1 Characterization of the scaffolds

The SEM images of the PADM scaffold are presented in Fig. 1a and b. The results indicate that the PADM scaffold is white

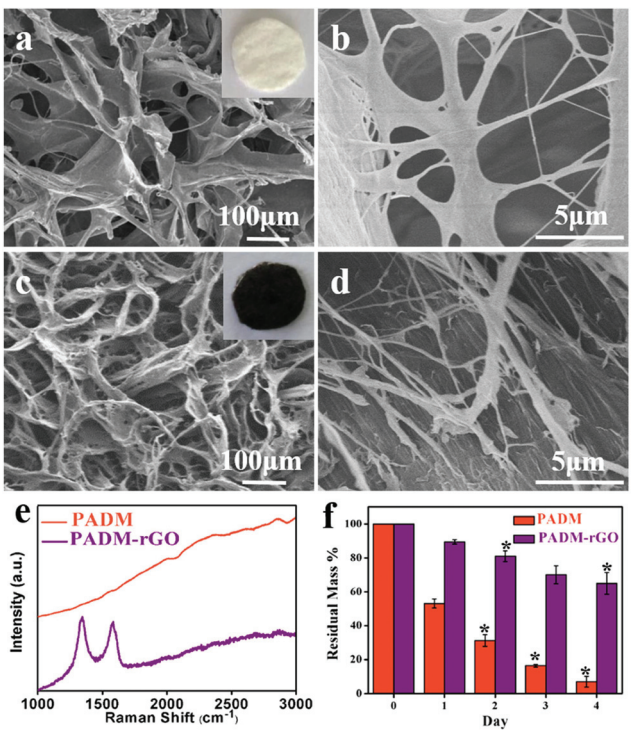

Fig. 1 Characterization of the PADM and PADM–rGO scaffolds. SEM images of the topography of PADM (a, b) and PADM–rGO (c, d), the (a-inset) and (c-inset) are photographs of PADM and PADM–rGO with 8 mm diameter, respectively. (e) Raman spectra (514 nm) of the two scaffolds. (f) The percentage of the residual mass of the PADM and PADM–rGO after enzymatic degradation at different time points. (*$p \leq 0.05$, **$p \leq 0.01$, $n = 3$).

(Fig. 1a-inset) and has a typical porous 3D structure with pores ranging from 50 to 150 μm, which is favorable for cell perfusion into the interior of the scaffold. As shown in Fig. 1b, the surface of the channel walls of the PADM collagen is smooth. From the digital pictures of the scaffolds, we can see that the color of the PADM changes from white to black after the rGO assembly (Fig. 1c-inset), and the PADM–rGO scaffold becomes conductive, as confirmed by the *I–V* test (Fig. S4†). Fig. 1c and d are the SEM images of the PADM–rGO hybrid scaffold. The topography and structure are not obviously changed after the assembly of a layer of the rGO film, including the channel wall surfaces. From the SEM images of ascorbic acid reduced GO (Fig. S3a†), and the channel surface of the PADM–rGO hybrid scaffold (Fig. S3b†), they have similar surface topographies, it could be demonstrated that the rGO film is well covered on the surface of the PADM.

The zeta potential of GO and PADM has a large gap of approximately 30.74 mV (Fig. S5a†); the GO sheets can thus be easily adhered onto the surface of the PADM and spread, and ascorbic acid, not only acting as a green reducing agent but also providing an acid environment for the esterification reaction between collagen and GO, makes the rGO nanosheets more stable on the surface of PADM (Fig. S2a†). From Fig. S2b,† the state of rGO was stable after the GO was reduced by ascorbic acid; it also demonstrated that once the GO adhered on the surface of PADM, besides the chemical bonding between the rGO and PADM, the adsorption capacity of the rGO film on the PADM surface is another guarantee of the rGO film being stable on PADM. PADM is a collagen-based material that possesses three characteristic amide band FT-IR spectrum absorbance peaks: amide I at 1660 cm^{-1}, amide II at 1550 cm^{-1} and amide III at 1240 cm^{-1}. The amino group absorbance peak (3300–3400 cm^{-1}) appears after the cross-linking process (Fig. S5b). With the rGO assembled on the surface of the PADM, some amide absorbance peaks are concealed, and the C=C absorbance peak is evident at 1650 cm^{-1}. A Raman spectrum is the most powerful tool to detect the presence of graphene; the Raman spectra of graphene include the G peak located at ~1580 cm^{-1}, caused by the in-plane optical vibration (degenerate zone center E^2_g mode), and the D peak, located at ~1350 cm^{-1} due to first-order zone boundary phonons.[31] As shown in Fig. 1e, the Raman spectrum of the PADM–rGO has two broad peaks, the ratio of $\frac{1D}{1G}$ is approximately 0.91, the ratio of $\frac{1D}{1G}$ of highly reduced GO sheet–PADM is 0.80 (Fig. S3c†); the defects make the ascorbic acid reduced GO film have a better adhering ability with proteins. Because of the absence of rGO, there is no characteristic peak for the PADM scaffold. Both the FT-IR spectrum and Raman spectrum indicate the successful assembly of the rGO film on the surface of PADM.

Fig. 1f illustrates the biodegradation behaviors of the PADM and PADM–rGO scaffolds. The results indicate that both of the scaffolds are biodegradable. After 1 day of enzymatic degradation, the residual mass of the PADM is approximately 53.05 ± 2.61%, but the residual mass of the PADM–rGO is approximately 89.45 ± 1.30%. The residual mass of both scaffolds decreased with an increase in enzymatic degradation time. After 4 days, the residual mass of the PADM was only approximately 7.09 ± 3.2%, but the PADM–rGO remained at 65.01 ± 6.42%, which indicates that rGO can delay the biodegradation period of PADM. Because neural regeneration is a long process,[3] this result suggests that the PADM–rGO hybrid scaffold with a lower degradation rate could be consistent with the neural regeneration process.

The characteristics of the two scaffolds suggest that these materials are good candidates for neural tissue engineering. The main purpose of this research was to investigate the effect of the two scaffolds on the neural differentiation of MSCs.

2.2 Cytocompatibilities of the scaffolds and cell attachment to the scaffolds

To study the response of MSCs to the two scaffolds, the cytocompatibility of the scaffolds was determined using isolated MSCs (the purity of the MSCs was above 90%, as illustrated in Fig. S6†). Third-passage cells were seeded on the PADM and PADM–rGO scaffolds at a density of 5×10^4 cells per dish. Live/dead cellular staining was assayed 24 h after the MSCs were seeded on the PADM and PADM–rGO scaffolds. The fluorescent images of the live/dead-stained MSCs on the PADM (Fig. 2a–c) and PADM–rGO (Fig. 2d–f) scaffolds illustrate that a high percentage of the seeded cells survive on the scaffolds, which suggests that both the PADM and PADM–rGO scaffolds have great biocompatibility. The morphology of the MSCs on the scaffolds after 1 day was also observed *via* actin staining (Fig. S7†). The cells on both of the scaffolds maintained the typical spindle shape. The proliferation of MSCs on the scaffolds was also assessed after cultivation of the cells for 1, 3, and 5 days. As depicted in Fig. S8,† the proliferation rate of the MSCs on the PADM–rGO scaffold was somewhat higher than that on the pure PADM scaffolds. A more detailed observation of cell proliferation was provided by the 2D CLSM fluorescence morphologies of the actin cytoskeletons of the MSCs cultured on PADM and PADM–rGO (Fig. S7†) after 1 day. The cell quantity increased rapidly on both scaffolds after 3 days, and the cells on the PADM–rGO hybrid scaffold had a higher proliferation rate. After 5 days, the cell quantities had nearly completely plateaued on the PADM and PADM–rGO hybrid scaffolds. This result suggests that the beginning of the neurogenesis process occurs at day 3 after cell seeding.

After normal culture of the MSCs on the scaffolds for 3 days, immunofluorescence and SEM observations were performed to examine the morphology of the MSCs. By labeling the actin cytoskeleton with phalloidin, the attachment and morphological characteristics of the MSCs on the PADM scaffold are revealed in typical 2D structure fluorescence micrographs (Fig. 2g). The cells spread well on the PADM channels and maintained the typical spindle shape. As shown in Fig. 2i, the cell density on the PADM–rGO hybrid scaffold was slightly higher. This result was confirmed in the 3D structure fluorescence micrographs of the MSC actin filaments

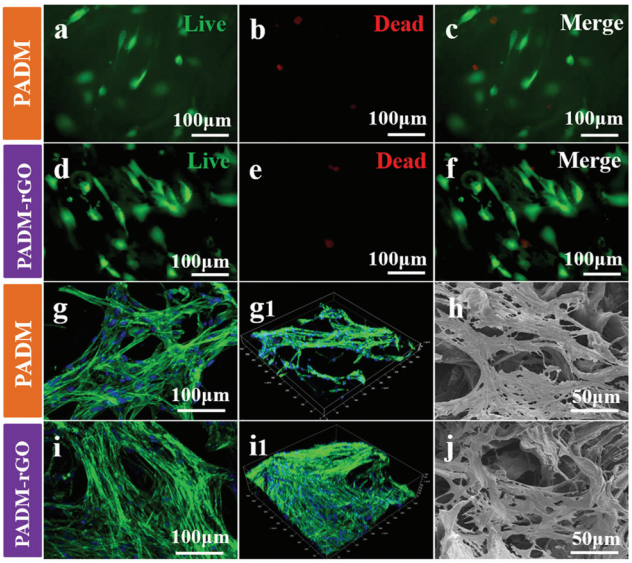

Fig. 2 The cytocompatibilities of the two scaffolds. Live/dead cellular staining was performed 24 h after the MSCs were seeded on the PADM (a, b, c) and PADM–rGO (d, e, f). The live cells are stained green, and dead cells are red. The 2D structures of CLSM fluorescence morphologies of the actin cytoskeleton of the MSCs cultured on the PADM (g) and PADM–rGO (i) scaffolds after normal culture for 3 days. The actin filaments of the cells were stained with Alexa-Fluor 488-phalloidin (green), and the nuclei were stained with DAPI (blue). 3D structures of the CLSM fluorescence morphologies of the MSC actin filaments on the PADM (g1) and PADM–rGO (i1) reveal the 3D cell culture framework of the scaffolds. SEM images indicate the typical cell attachment of the MSCs after 3 days on the PADM (h) and PADM–rGO (j).

(Fig. 2g1 and i1). This result demonstrates that a layer of rGO assembled on the surface of PADM will promote cell attachment and proliferation. After reduction, rGO retains a few oxygen-containing groups, which can adhere serum proteins and endows the scaffold with an improved cell attachment ability.[21] In addition, the typical 3D structure in the CLSM images of the actin filaments demonstrates that the cells not only attach onto the surface of the scaffold but also migrate into the inner pores of the two scaffolds (Fig. S9a and S9b†). The depth of the ingrowth of the cells can reach approximately 160 μm. SEM images of MSCs cultured on the PADM (Fig. 2h) and PADM–rGO (Fig. 2i) exhibit the normal attachment behavior after 3 days of normal culturing. The SEM images reveal that most of the area of the surface of the PADM and PADM–rGO scaffolds is covered with the cells. Previous studies have demonstrated that hydrophilic GO could contribute a more appropriate environment for cell attachment and growth by combining the serum proteins.[32]

Moreover, the above results indicate that, with normal culturing of MSCs on the two scaffolds, there is no cytotoxicity, and the assembly of a layer of rGO on the surface of the PADM could promote the attachment and proliferation of MSCs. Therefore, PADM–rGO is an ideal candidate scaffold to study the effect on MSC neural differentiation.

2.3 Neural differentiation of MSCs on the scaffolds

The MSCs were cultured on the PADM and PADM–rGO scaffolds under neurogenic conditions for 7 days. The differentiated cells were observed after immunostaining for the early neural markers Nestin, β-Tubulin III (Tuj1) and GFAP and the later neural marker, MAP2. The neural-like cells were observed on both scaffolds.

Compared to that of the cells on the PADM scaffold (Fig. 3a and a1), the Nestin expression of the cells on the PADM–rGO scaffolds is much stronger (Fig. 3e and e1). For the neuronal specific markers Tuj1 and MAP2, Fig. 3f, f1, h and h1 illustrate a significant increase of positive cells on the PADM–rGO scaffold compared with the PADM scaffold (Fig. 3b, b1, d and d1). For the glial marker GFAP, there is a slight decrease in the cells on the PADM–rGO (Fig. 3g and g1) compared with the cells on the PADM scaffold (Fig. 3c and c1), which is not a negative result. These results suggest that the PADM–rGO scaffold could specifically enhance MSC neural differentiation compared to the PADM scaffold.

To further confirm these results, a qPCR assay was performed to analyze the neuronal gene expression levels after MSC neurogenesis for 7 days. The sequences of the real-time PCR primers are shown in Table S1.† Compared with the cell differentiation on the PADM scaffold, the changes in Nestin, Tuj1 and MAP2 expression in the cells differentiated on the PADM–rGO hybrid scaffold were 2.597 ± 0.422-fold, 5.987 ±

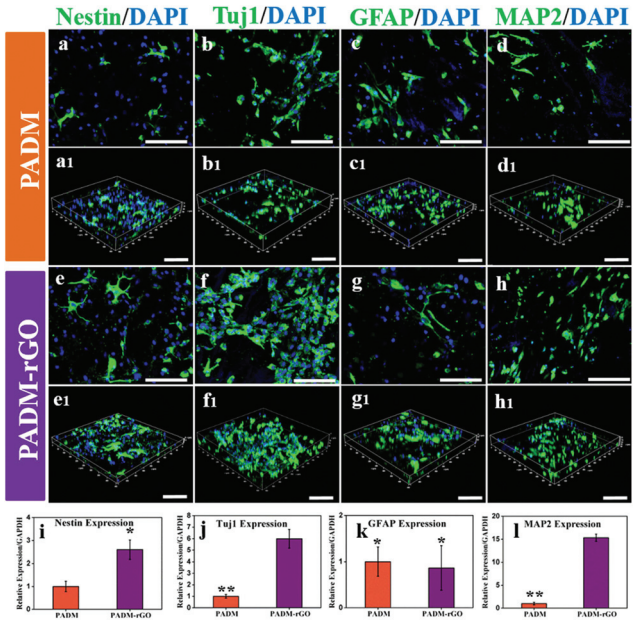

Fig. 3 Neural marker expression of MSCs under neurogenesis conditions for 7 days. 2D and 3D CLSM fluorescence micrographs of immunostained cells on the PADM (a–d1) and PADM–rGO scaffolds (e–h1). Nestin, Tuj1, GFAP and MAP2 are shown in green, and the nuclei were stained with DAPI (blue) (scale bar = 100 μm). qPCR analysis of the expression levels of the neural-specific genes Nestin (i), Tuj1 (j), GFAP (k), and MAP2 (l) on the PADM and PADM–rGO scaffolds, respectively. (*$p \leq 0.05$, **$p \leq 0.01$, $n = 3$).

0.826-fold and 15.321 ± 0.804-fold, respectively (Fig. 3i, j and l), which indicates a significant increase in neuronal differentiation on the PADM–rGO scaffold. The GFAP expression on the PADM–rGO scaffold was 0.864 ± 0.048-fold lower than on the PADM scaffold (Fig. 3k). These results also confirmed that the PADM–rGO scaffold can specifically increase neuronal gene expression.

The flexibility, stiffness, dimensions, topographical and electrical properties of the scaffolds could be the biological effects that regulate the fate of stem cells. Neural cells are electro-active ones and the bio-electronic interface can affect neural cell behaviors; graphene can match the charge transport demand for electrical cellular interfacing applications to regulate nerve cell behaviors, which makes it a promising candidate as a neural interfacial material. These results demonstrate that with a layer of rGO nanosheets assembled on the surface of the PADM channels, the good conductivity of the PADM–rGO scaffold is a positive influence on the differentiation of MSCs into neural cells as assessed by protein and gene expression levels and promotes a faster maturation rate of the neural cells.

To characterize the effect of the PADM and PADM–rGO scaffolds on differentiated MSC neurite sprouting and outgrowth, the cell morphologies were observed *via* SEM after the MSCs were exposed to neurogenic conditions for 7 days. In the SEM images of the neural-induced MSCs on the PADM (Fig. 4a and b) and PADM–rGO (Fig. 4c and d), the MSCs had differentiated into cells with neural morphology. The length of the differentiated cellular neurites on the PADM–rGO hybrid scaffold was over 100 μm, which is much longer than the neurite length on the PADM scaffold. Fig. 4c and d also show a more powerful adhering property of PADM–rGO than PADM for serum proteins.

Neural cells in the early development stage are more sensitive to the surrounding physical cues, and the ability to utilize physical cues such as topographical features, substrate stiffness, electric conductivity and the dimensions of the ECM to regulate stem cell fate has great potential in regenerative medicine.[33] A neurite refers to any projection from the cell body of a neural cell. This projection can be either an axon or a dendrite. Neurite sprouting and outgrowth is one of the most important phenomena in the development of the nervous system. The PADM–rGO hybrid scaffold possesses an enormous interface with high conductivity for bioelectricity and is thus promising in the development of a much better bioelectric interface to enhance the differentiation of MSCs into neural cells compared to the PADM scaffold. It is interesting to note that the topography of PADM–rGO with bundled collagen fibers may mimic the surrounding ECM of neural cells, which might provide another cue to make the scaffold a more positive substrate for neural cell growth.

Above all, these findings indicate that the incorporation of a layer of graphene on PADM provides specific cues to MSCs, resulting in enhanced cell–cell communication. The results suggest that graphene with good electrical conductivity may promote the differentiation of MSCs into neural cells. Without a significant change in the surface topography after assembling a layer of the rGO film on the PADM channels, we can ensure that the differentiation of MSCs into neural cells induced on the graphene-based platform is not due to the effects such as stiffness and roughness.

According to this sample method, assembling a small amount of graphene on the channel surface of porous 3D PADM is an effective approach for designing a graphene-based, conductive, porous 3D scaffold in the field of neural regeneration. Our method may also allow the fabrication of other 2D or 3D graphene-based scaffolds using a combination of convenient biomaterials.

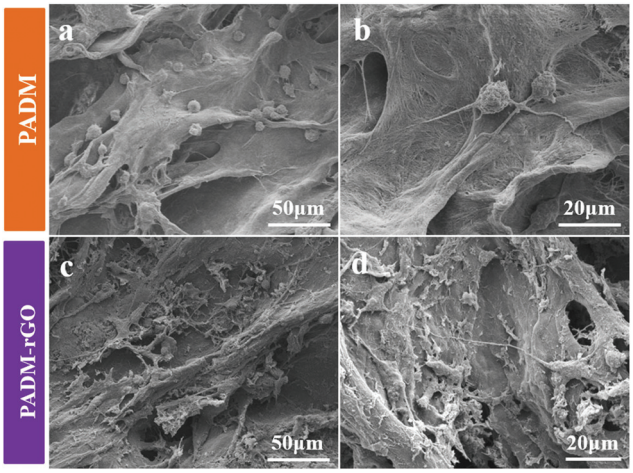

Fig. 4 SEM images showing the typical neurite sprouting and outgrowth of the MSCs after 7 days under neurogenic conditions on the PADM scaffold (a), (b) and the PADM–rGO hybrid scaffold (c), (d).

3. Conclusion

In summary, engineering scaffolds to regulate the cellular behaviors of stem cells into desired cell phenotypes and genotypes is the most critical factor in scaffold design for tissue engineering applications. Our findings reveal that with a layer of the rGO film assembled on the surface of PADM channels, the conductivity of the PADM–rGO scaffold can not only support MSC attachment but also maintain cells in a more active proliferation and neural differentiation state, with the up-regulation of Nestin, Tuj1 and MAP2 protein and gene expression. The rGO on the channel surface of 3D PADM can more efficiently promote neurite sprouting and outgrowth than the PADM scaffold under neurogenic conditions for 7 days. Due to these interactions of rGO and PADM with neural cells, it may be potentially used as an implant material to provide an ideal scaffold with a porous 3D structure and excellent biocompatibility, controlled biodegradability, and conductivity for neural tissue engineering.

4. Experimental section

4.1 Preparation of the PADM scaffold

The PADM was prepared by the procedure described in our previous work.[34] To obtain a long-term performance regarding biodegradation and endow the PADM with greater strength, the as-prepared PADM was cross-linked by immersing the PADM sheet into a mixed solution containing 10 nm 1-ethyl-3-(3-dimethylaminopropyl)carbodiimide hydrochloride (EDC) and *N*-hydroxysuccinimide (NHS) (Alfa Aesar, Tianjin) with a molar ratio of 2.5 : 1 (EDC : NHS).[35] The EDC/NHS cross-linking process serves to reinforce the decellularized organ matrix, and EDC is a zero-length cross-linker which does not form harmful crosslink bonds. Our previous work demonstrated that the mechanical strength of the PADM is greatly improved and the biodegradation rate is decreased by this cross-linking process. The PADM thickness was 0.2–0.3 mm, and the PADM was sliced into disks 8 mm in diameter for the following experiments.

4.2 Preparation of an aqueous solution of GO

The GO was prepared by the modified Hummers' method. Briefly, graphite powder was pre-treated with concentrated H_2SO_4, $K_2S_2O_8$ and P_2O_5. Then, the pre-treated graphite powder was oxidized with concentrated H_2SO_4 and $KMnO_4$ *via* the traditional Hummers' method. More detailed procedures can be found in ESI S1.†

4.3 Preparation of the PADM–rGO hybrid scaffold

GO nanosheets were assembled on the PADM scaffold by a solution immersion process and then reduced with ascorbic acid *in situ* as follows. The PADM disk was placed in a polyethylene (PE) tube with 4 ml of a 0.25 mg per ml GO solution and immersed for 12 h. Then, 1 ml of a 10% ascorbic acid solution was added to the tube, which was incubated in a 50 °C water bath overnight for reduction. After the above process, the white PADM disk turned black, and the samples were soaked in deionized water for 1 h and washed carefully. After 4 washes, the PADM–rGO scaffolds were obtained and collected for cell culture.

4.4 *In vitro* enzymatic degradation studies

The biodegradation stability of the PADM samples was measured by exposing the scaffold to 1 ml of collagenase (12.5 U ml^{-1}) (Sigma). The PADM–rGO samples were first exposed to 1 ml of 12.5 U per ml collagenase for 12 h and then exposed to 1 ml of horseradish peroxidase (HRP) (Aladdin) (50 U ml^{-1}) for an additional 12 h. The enzymatic treatment alternated every 12 h. At 24, 48, 72 and 96 h, the degradation rate of the samples was evaluated. The stability of the PADM and PADM–rGO scaffolds to biodegradation was assessed by calculating the percentages of the remaining weight after enzymatic degradation at different time points.

4.5 Microstructural characterization of the samples

The topography of the samples was characterized *via* SEM (SU8020, Hitachi, Japan). A Dilor XY microspectrometer with 532 nm laser excitation was used to record the Raman spectra of the PADM–rGO samples. The 3D scanning immunofluorescence micrographs were captured with a Leica SP8 confocal laser scanning microscope (CLSM) in a z-stack model.

4.6 Cell culture

MSCs were isolated from the femurs and tibias of four-week-old male Wistar rats, as previously described. The cells were cultured in primary medium containing low glucose (1.0 g l^{-1}) Dulbecco's modified Eagle's medium (L-DMEM, Gibco) supplemented with 10% fetal bovine serum (FBS, Gibco), 1% penicillin–streptomycin (Gibco), and 4 ng per ml basic fibroblast growth factor (bFGF). MSCs at the third to eighth passage were used for all of the following experiments.

4.7 Neural differentiation of MSCs on the scaffolds

The neural differentiation of the MSCs was induced under the following neurogenic conditions: after the first 3 days, the basal culture medium of the rMSCs was replaced with neural differentiation medium DMEM/F12 (Gibco) containing 20 ng per ml bFGF (Peprotech), 10 ng per ml human nerve growth factor (NGF, Peprotech), 10 ng per ml human brain-derived neurotrophic factor (bDNF, Peprotech), 2% B27 supplement (Invitrogen) and 1% penicillin–streptomycin (Gibco). The culture medium was replaced every two days.

4.8 Cell morphology

The morphology of the cells cultured on the different samples 24 h after seeding the cells or after 7 days of neural induction was observed *via* SEM (Hitachi; SU8020). The cell-seeded scaffolds were removed from the culture medium and gently washed with Dulbecco's phosphate-buffered saline (DPBS). The cells on the scaffolds were fixed with 4% paraformaldehyde in PBS for 2 h at room temperature. After removing the fixative, the scaffolds were gently washed with PBS and immersed in 1% w/v osmic acid for 2 h. After washing, the scaffolds were subjected to sequential dehydration for 15 min twice each with an ethanol series (30%, 50%, 70%, 85%, 90%, 95%, 98% and 100%). After lyophilization and coating with gold, the scaffolds with the cells were observed by SEM to assess cell attachment and morphology at 5 kV accelerating voltage.

4.9 Cell viability assay on PADM and PADM–rGO

MSCs were seeded on the PADM and PADM–rGO scaffolds. After 1 day of culture, a cell viability assay was performed using the LIVE/DEAD Cell Imaging kit for mammalian cells (Life Technology) according to the manufacturer's instructions.

4.10 Immunofluorescence

To investigate the cellular attachment on PADM and PADM–rGO, the MSCs on the samples were imaged with the immunofluorescence measurement of F-actin after 3 days of culture. Briefly, the cells were washed with PBS, fixed with 4% paraformaldehyde solution in PBS for 20 min, washed with PBS three times, extracted with 0.1% Triton X-100 (Sigma) for 10 min and blocked with 5% bovine serum albumin (Sigma) for 30 min. The cells were then stained with phalloidin conjugated to Alexa Fluor 488 (Invitrogen) at a 1 : 200 dilution for 60 min to stain the actin filaments, and the nuclei were stained with 4′,6-diamidino-2-phenylindole (DAPI, 300 nM, Life Technology) for 10 min. Finally, the cells were washed with TPBS three times before examination with a Leica confocal microscope SP8.

After culturing for 7 days in the neural differentiation medium, the scaffolds with the cells were washed with PBS, fixed in 4% paraformaldehyde for 40 min, extracted with 0.1% Triton X-100 (Sigma) for 10 min and blocked with 10% goat serum (Sigma) for 2 h. The samples were incubated with the primary antibodies overnight at 4 °C and then incubated for 2 h at room temperature with the secondary antibodies, followed by DAPI staining. The primary antibody panel included Alexa Fluor 488-conjugated anti-Nestin (1 : 200, Millipore), anti-Tuj1 (1 : 500, Abcam), anti-glial fibrillary acidic protein (GFAP) (1 : 500, Abcam), and Alexa Fluor 488-conjugated anti-microtubule-associated protein-2 (MAP2) (1 : 200, Millipore) antibodies. The secondary antibody was Alexa Fluor 488-conjugated goat anti-mouse IgG (1 : 200, Jackson ImmunoResearch).

4.11 qPCR

The RNA samples were extracted from the cells after 7 days of differentiation using an RNeasy Plus Mini Kit (Qiagen). The RNA was reverse-transcribed into cDNA using PrimeScriptTM (Takara). The total RNA concentration, purity, and integrity were determined using a spectrophotometer (Q-5000; Quwell) and agarose gel electrophoresis. The qPCR assay was performed with SYBR Premix Ex TaqTM (Takara) on an ABI 7500 Fast Real Time PCR system (Applied Biosystems) for one housekeeping gene, glyceraldehyde-3-phosphate (GAPDH), and four genes of interest, Tuj1, Nestin, GFAP, and MAP2 (see Table S1† for primer sequences). The relative transcript expression levels of the target gene were normalized to GAPDH and were expressed as the means ± standard deviation (SD) (n = 3 for each group).

4.12 Statistical analysis

The data were reported as the means ± SD, and the statistical analysis was performed using unpaired Student's t-tests. Statistical significance was accepted at $^{*}p \leq 0.05$ and $^{**}p \leq 0.01$.

Conflict of interest

The authors declare no competing financial interests.

Acknowledgements

The authors are thankful for funding from the National Natural Science Foundation of China (Grant No. 51402063), the China Postdoctoral Science Foundation (no. 2014M550673), the Fundamental Research Funds of Shandong University (2014QY003, 2014JC019) and the "100 Talents Program" of the Chinese Academy of Sciences. Thanks are also due to support from the "Thousands Talents" program for pioneer researchers and his innovation team, China.

References

1 X. Gu, F. Ding and D. F. Williams, *Biomaterials*, 2014, **35**, 6143–6156.
2 C. E. Schmidt and J. B. Leach, *Annu. Rev. Biomed. Eng.*, 2003, **5**, 293–347.
3 A. Subramanian, U. M. Krishnan and S. Sethuraman, *J. Biomed. Sci.*, 2009, **16**, 108.
4 S. J. Hollister, *Nat. Mater.*, 2005, **4**, 518–524.
5 G. A. Saracino, D. Cigognini, D. Silva, A. Caprini and F. Gelain, *Chem. Soc. Rev.*, 2013, **42**, 225–262.
6 X. Xu, W.-C. Yee, P. Y. Hwang, H. Yu, A. C. Wan, S. Gao, K.-L. Boon, H.-Q. Mao, K. W. Leong and S. Wang, *Biomaterials*, 2003, **24**, 2405–2412.
7 X. Jiang, S. H. Lim, H.-Q. Mao and S. Y. Chew, *Exp. Neurol.*, 2010, **223**, 86–101.
8 J. Undin, A. Finne-Wistrand and A.-C. Albertsson, *Biomacromolecules*, 2014, **15**, 2800–2807.
9 X. Li, C. Chu, L. Liu, X. Liu, J. Bai, C. Guo, F. Xue, P. Lin and P. K. Chu, *Biomaterials*, 2015, **49**, 135–144.
10 P. B. Malafaya, G. A. Silva and R. L. Reis, *Adv. Drug Delivery Rev.*, 2007, **59**, 207–233.
11 K. Leong, B. Brott and R. Langer, *J. Biomed. Mater. Res.*, 1985, **19**, 941–955.
12 S. Baiguera, C. Del Gaudio, E. Lucatelli, E. Kuevda, M. Boieri, B. Mazzanti, A. Bianco and P. Macchiarini, *Biomaterials*, 2014, **35**, 1205–1214.
13 H. C. Ott, T. S. Matthiesen, S.-K. Goh, L. D. Black, S. M. Kren, T. I. Netoff and D. A. Taylor, *Nat. Med.*, 2008, **14**, 213–221.
14 H. Zhao, G. Wang, S. Hu, J. Cui, N. Ren, D. Liu, H. Liu, C. Cao, J. Wang and Z. Wang, *Tissue Eng., Part A*, 2010, **17**, 765–776.
15 J.-K. Chai, L.-M. Liang, H.-M. Yang, R. Feng, H.-N. Yin, F.-Y. Li and Z.-Y. Sheng, *Burns*, 2007, **33**, 719–725.
16 M. Zhang, X. Huang and Y. Li, *J. Pract. Obstet. Gynecol.*, 2012, **8**, 014.
17 S. Y. Park, J. Park, S. H. Sim, M. G. Sung, K. S. Kim, B. H. Hong and S. Hong, *Adv. Mater.*, 2011, **23**, H263–H267.
18 L. Ghasemi-Mobarakeh, M. P. Prabhakaran, M. Morshed, M. H. Nasr-Esfahani, H. Baharvand, S. Kiani, S. S. Al-Deyab and S. Ramakrishna, *J. Tissue Eng. Regener. Med.*, 2011, **5**, e17–e35.
19 L. Feng, L. Wu and X. Qu, *Adv. Mater.*, 2013, **25**, 168–186.

20 W. C. Lee, C. H. Y. Lim, H. Shi, L. A. Tang, Y. Wang, C. T. Lim and K. P. Loh, *ACS Nano*, 2011, **5**, 7334–7341.
21 H. Y. Mao, S. Laurent, W. Chen, O. Akhavan, M. Imani, A. A. Ashkarran and M. Mahmoudi, *Chem. Rev.*, 2013, **113**, 3407–3424.
22 J. H. Wen, L. G. Vincent, A. Fuhrmann, Y. S. Choi, K. C. Hribar, H. Taylor-Weiner, S. Chen and A. J. Engler, *Nat. Mater.*, 2014, **13**, 979–987.
23 Y. Wang, W. C. Lee, K. K. Manga, P. K. Ang, J. Lu, Y. P. Liu, C. T. Lim and K. P. Loh, *Adv. Mater.*, 2012, **24**, 4285–4290.
24 P. Bianco and P. G. Robey, *Nature*, 2001, **414**, 118–121.
25 C. Toma, M. F. Pittenger, K. S. Cahill, B. J. Byrne and P. D. Kessler, *Circulation*, 2002, **105**, 93–98.
26 I. Aurich, L. P. Mueller, H. Aurich, J. Luetzkendorf, K. Tisljar, M. M. Dollinger, W. Schormann, J. Walldorf, J. G. Hengstler and W. E. Fleig, *Gut*, 2007, **56**, 405–415.
27 Y. Takashima, T. Era, K. Nakao, S. Kondo, M. Kasuga, A. G. Smith and S.-I. Nishikawa, *Cell*, 2007, **129**, 1377–1388.
28 S. Wislet-Gendebien, G. Hans, P. Leprince, J. M. Rigo, G. Moonen and B. Rogister, *Stem Cells*, 2005, **23**, 392–402.
29 J. Deng, B. E. Petersen, D. A. Steindler, M. L. Jorgensen and E. D. Laywell, *Stem Cells*, 2006, **24**, 1054–1064.
30 M. Matsumoto, T. Imura, T. Fukazawa, Y. Sun, M. Takeda, T. Kajiume, Y. Kawahara and L. Yuge, *Neurosci. Lett.*, 2013, **533**, 71–76.
31 K. N. Kudin, B. Ozbas, H. C. Schniepp, R. K. Prud'Homme, I. A. Aksay and R. Car, *Nano Lett.*, 2008, **8**, 36–41.
32 N. Li, Q. Zhang, S. Gao, Q. Song, R. Huang, L. Wang, L. Liu, J. Dai, M. Tang and G. Cheng, *Sci. Rep.*, 2013, **3**, 1604.
33 T. Dvir, B. P. Timko, D. S. Kohane and R. Langer, *Nat. Nanotechnol.*, 2011, **6**, 13–22.
34 J. Qiu, J. Li, G. Wang, L. Zheng, N. Ren, H. Liu, W. Tang, H. Jiang and Y. Wang, *ACS Appl. Mater. Interfaces*, 2012, **5**, 344–350.
35 J. Li, N. Ren, J. Qiu, H. Jiang, H. Zhao, G. Wang, R. I. Boughton, Y. Wang and H. Liu, *Int. J. Biol. Macromol.*, 2013, **61**, 69–74.

